Dissimilar substitution : A facile route to synthesize transition metal dichacolgenide alloys and heterostructures

Sandhya Susarla,[a,†] Vidya Kochat,[a,*,†] Alex Kutana,[†] Jordan A. Hachtel,[‡] Juan Carlos Idrobo,[‡] Robert Vajtai,[†] Boris I. Yakobson,[†] Chandra Sekhar Tiwary,[†] and Pulickel M Ajayan[*,†]

†*Materials Science and Nano Engineering, Rice University, Houston, TX 77005, USA*
‡*Center for Nanophase Materials Sciences, Oak Ridge National Laboratory, Oak Ridge, TN 37831, USA*

E-mail: vidya.kochat@rice.edu; ajayan@rice.edu

---

[a] These authors contribute equally to this work.
[a]

Abstract

Transition metal dichalcogenide alloys form a broad class of 2D layered materials with tunable bandgaps leading to interesting optoelectronic applications . In the bottom-up approach of building these atomically thin materials, atomic doping plays a crucial role. Here we demonstrate a single step growth procedure for obtaining uniform binary alloys and heterostructures by tuning atomic composition. We show that very minute doping of tin during the growth phase of $Mo_{1-x}W_xS_2$ alloy system leads to phase separation of the alloy regions to almost pure phases and promotes lateral and vertical heterostructure growth. HAADF-STEM imaging and DFT calculations also support the modified stacking and growth mechanism due to the non-isomorphous Sn substitution. Our experiments demonstrate the possibility of growing heterostructures of TMD alloys whose spectral responses can be desirably tuned for various optoelectronic applications.

2D semiconducting transition metal dichalcogenides (TMDs) are an interesting class of 2D materials due to their layered structure, band gaps varying from direct to indirect with increase in layer number and reasonable room temperature carrier mobilities which have a great potential in low-power, flexible optoelectronics.[1] Their high quantum efficiency and optical absorption even for monolayer thickness have led to the demonstration of various applications as photodetectors, photovoltaic cells and light emitting diodes.[2] These properties have led to further research to engineer the optical band gap of the TMD materials by introducing strain,[3–5] alloying[6–14] and building heterostructures.[15–17] Controlled straining of atomically thin TMDs poses challenges in wide tunability. The heterostructures of 2D TMDCs constructed by layer-by-layer mechanical stacking and epitaxial growth by chemical vapor deposition have been shown to result in Type-II band alignment and host inter-layer excitons having long lifetimes.[16,18] These vertical heterostructures have led to the development of atomically thin solar cells with high quantum efficiency.[19] Alloying of the TMDs provides freedom and control to tune the structure and properties. Alloy compositions of M(=Mo, W) and X(=S, Se) have also been theoretically predicted to be stable thermodynamically and exhibit band gap modulation depending on the concentration of the various constituent atoms.[6–8,10–12,14] These alloys also offer versatility in engineering the spin-orbit coupling, which influences the population of bright and dark excitons leading to changes in light emission intensity, which is a desired property in the design of LEDs.[20] They also show a non-linear variation in the degree of valley polarization based on their composition which can be utilized in valleytronics-based devices.[20]

The 2D TMD alloys have been mainly synthesized as bulk crystals using chemical vapor transport followed by micromechanical exfoliation to thinner layers.[12,14,20,21] Even though this technique offers very good composition tunability, it does not yield large-sized flakes required for the envisioned optoelectronic applications. An alternate technique of sulphurization of $\mathrm{Mo}_{1-x}\mathrm{W}_x\mathrm{O}_y$ alloy thin films grown by super-cycle ALD has also been explored which has led to the growth of large area 2D alloys.[7] Chemical vapor deposition has already been established as a facile route to grow 2D transition metal dichalcogenides with high quality and lateral sizes[22–24] and has been recently explored to synthesize the alloys of TMDs as well.[6,8,25,26] The structural characterization studies reveal isomorphous substitution of Mo and W (S and Se). In the current work we demonstrate how non-isomorphous substitution of a ternary metal precursor can lead to phase separation in a 2D binary alloy system of $Mo_{1-x}W_xS_2$ and increase the growth kinetics in the out-of-plane direction resulting in a layered structure of alloy heterostructures. DFT-based calculations are performed to get insights into the possible growth mechanisms.

The 2D binary alloys of $Mo_{1-x}W_xS_2$ were grown at 800^0C from a homogeneous mixture of MoO_3 and WO_3 taken in known weight ratio (1:2, 1:4 and 1:6) and sulphur in the presence of continuous Ar gas flow (See supplementary information). The compositions are chosen keeping in mind that MoO_3 has a higher vapor pressure than WO_3. The composition of W in this alloy is tuned by increasing the mole fraction of WO_3 in the precursor mixture. Mo and W mix isomorphously leading to 2D $Mo_{1-x}W_xS_2$ alloys with well-defined compositions. The optical micrographs and AFM images of such alloys obtained by changing the weight of MoO_3 and WO_3 in the precursor mixture in the ratios of 1:2, 1:4 and 1:6 are shown in Fig. 1b and d respectively. In general we observed monolayer growth followed by second layer growing from a random distribution of secondary nucleation sites. Following this we introduced an additional element, Sn, to the growth atmosphere of the binary TMD alloys. We select Sn because it is distinct from the elements in the transition metal family. Also, SnS_2 crystallizes in CdI_2-type crystal structure ($a = 3.65$Å, $d_{S-Sn} = 2.57$Å), which is different from MoS_2 and WS_2 structures ($a = 3.15$Å, $d_{S-Sn} = 2.42$Å) and has an indirect bandgap for bulk as well as monolayer flakes.[27] These considerations show that Sn would give rise to non-isomorphous substitution in MoS_2 and WS_2 lattice and it would be interesting to investigate the stability of such an alloy system and its properties. Growth was carried out with different ratios (1:2:8, 1:4:8, and 1:6:8) of MoO_3, WO_3 and SnO_2 under identical conditions. The optical and AFM images of the 2D crystals obtained from these growths are shown in Fig. 1c and e respectively. Unlike in the case of binary alloy of $\mathrm{Mo}_{1-x}\mathrm{W}_x\mathrm{S}_2$ which had random secondary nucleation sites, the crystals grown from ternary metal precursors grew in a layered structure as seen from the optical and AFM studies indicating entirely different growth kinetics.

The composition of the various binary and ternary alloys was investigated using Raman and photoluminescence studies, X-ray photoelectron spectroscopy and HR STEM imaging. The unpolarized Raman and PL maps with 532 nm excitation for the samples grown from the binary precursor mixtures are shown in Fig. 2a-c. For the samples grown with the precursor weight ratio of 1:2, the Raman spectra (Fig. 2a(ii)) obtained at the center showed peaks at 381 cm^{-1} and 405 cm^{-1} corresponding to E_{2g}^1 and A_{1g} modes of MoS_2,[28] whereas at the edges additional peaks were observed at 350 cm^{-1} and 417 cm^{-1} representing the WS_2-like $2LA(M) + E_{2g}^1$ and A_{1g} modes respectively.[29] The Raman maps at 350 cm^{-1} (green) and 381 cm^{-1} (red) shown in the inset and the combined PL map of peaks at 1.82 eV (red) and 1.90 eV (green) plotted in Fig. 2a(iii) clearly reveal WS_2-like modes developing at the edges. The well-defined boundary seen in the Raman and PL maps along with the AFM images in Fig. 1d showing zero step height within the flakes are indicative of a lateral heterostructure evolution in these flakes. On increasing the WO_3 ratio to 1:4, we observe uniform Raman spectra across the whole sample as shown in Fig. 2b(i) which contains both the MoS_2-like and WS_2 like modes clearly identified in the Raman maps at 350 cm^{-1} (green) and 405 cm^{-1} (red) in Fig. 2b(ii). The PL map at 1.85 eV shown in Fig. 2b(iii) exhibits a central low intense region surrounded by a relatively larger intensity region. The PL peak at the central regions was found to be blue-shifted to 1.87 eV and could be attributed to the defects like S vacancies during the initial stage of growth.[30,31] The secondary nucleation sites of bilayer regions are clearly distinguishable from the quenched regions in the PL map. On further increase in the ratio of WO_3 precursor to 1:6, we again obtained lateral heterostructures indicated by a clear peak shift in PL from 1.82 eV at the center to 1.9 eV at the edges as shown in Fig. 2c(iii). The Raman spectra (Fig. 2c(i)) and AFM images also confirm the formation of this type of lateral heterostructure as the central region exhibits both MoS_2-like and WS_2-like Raman peaks whereas the edges have predominantly peaks from WS_2, implying the reverse growth scenario from that in 1:2 ratio. These observations clearly point to the fact that at the fixed growth temperature of 800^0C, the difference in the sublimation rates of MoO_3 and WO_3 can be utilized along with tuning the precursor ratio to obtain uniform alloys and lateral heterostructures of binary alloys.

The atomic structure of these alloys was studied using an aberration-corrected scanning transmission electron microscope (STEM) operated at an accelerating voltage of 60 kV.[32] Fig. 2d(i) shows a high angle annular dark field (HAADF) STEM image of a large region of a bilayer binary alloy grown from 1:4 precursor ratio. In HAADF imaging, the primary contrast mechanism is Z-contrast, meaning elements with higher atomic numbers (higher Z) exhibit higher intensity in the HAADF image. As a result, Mo and W atoms can be distinguished based on the difference in intensity between atomic columns in the HAADF-STEM image. To determine the composition of the sample from the HAADF image, a relative intensity threshold is needed to distinguish between Mo and W atoms. A higher magnification view of the HAADF image in Fig. 2d(i) is shown as an inset, along with a line profile of the inset image directly below. However, the line profile shows that there are not two discrete HAADF intensities corresponding to each of the two metals, but rather a quasi-continuous spectrum of intensities. There are three possible reasons for the lack of discrete Mo and W peaks beyond simple signal-to-noise errors in the image acquisition: carbon contamination, W mobility, and intermediate Z-contrasts. The sample is not perfectly clean, and hydrocarbon contamination can build up on the surface, which alters the detected HAADF intensity without affecting the genuine composition. Additionally, the W atoms are mobile under electron irradiation, which raises the issue of an atom jumping mid-scan. To mitigate this issue the STEM images are acquired by taking multiple frames with fast scan parameters and then summing them to enhance the signal-to-noise ratio, but this means that W atoms can contribute partial intensity to multiple sites broadening the detected W signal in the intensity histogram. Lastly, since the alloy is bilayer, there are likely many columns with one Mo and one W atom (as opposed to pure Mo and pure W), providing an intermediate Z-contrast level that fills in the gap between Mo and W in the histogram. Fig. 2d(ii) shows a histogram of the intensities of all the atoms in the image, and as expected from the line profile in (i), there is not a clear point where the Mo intensities and the W intensities begin. The continuous intensity distribution in the image precludes rigorous quantification, however the atoms can be labeled by setting an approximate threshold to obtain a qualitative picture of how W atoms are distributed in the bilayer. The threshold is chosen such that it captures the brightest atoms in the HAADF as W and the dimmer atoms as Mo. The value of the threshold was changed until the atom-labeled image shown appeared to most accurately represent the original HAADF image, which occurs at a relative intensity threshold of 0.36, the atom labeled image for this threshold is shown in Fig. 2d(iii). The resulting concentration from the STEM quantification is W-985 atoms (17.2%) and Mo-4736 (82.8%). The atom-labeled image shows that the W atoms are distributed in isolated packets throughout the bilayer, as opposed to being uniformly alloyed throughout the sample.

Following this the composition analysis and characterization of the ternary alloys were carried out to understand the non-isomorphous Sn substitution growth scenario. For the growth where the Mo,W and Sn precursor weight ratio was 1:2:8, we obtained layer-by layer growth, with thicker crystal growth at the edges. The PL spectra acquired at the centre (red) and the edges (black) showed peak positions at 1.83 and 1.9 eV respectively (Fig. 3a(i)). The Raman spectra and maps at 350 cm^{-1} and 405 cm^{-1} revealed MoS_2-like peaks at the center and WS_2-like peaks at the edges as shown in Fig. 3a(ii). This clearly indicates phase separation of MoS_2 and WS_2 at the edges unlike the binary alloys. For the growth where the WO_3 weight was doubled (1:4:8), we observe layer-by-layer growth nucleating from the center of the first grown layer. The Raman spectrum of the bottom layer (marked in black) showed Mo-dominant alloy, while the second layer has Mo-dominated center with increasing W towards the edges as can be seen from Fig. 3b(ii). The PL spectra shown in Fig. 3b(iii) shows two peaks at 1.81 and 1.98 eV corresponding to the A-excitonic peaks of MoS_2 and

WS_2. The observation of two separate peaks indicates microscopic phase separation of the Mo and W regions. For further increase in the weight ratio of WO_3 (1:6:8), we observe multilayer growth of W-dominated alloys with secondary layers nucleating from the center of the primary layer as can be seen from the PL map at 1.94 eV shown in Fig. 3c(ii) and the Raman spectra and map at 350 cm^{-1} shown in Fig. 3c(iii). In the region of the second layer, the PL is quenched and the intensity ratio of the $2LA(M)/A_{1g}$ mode is reduced. The Raman and PL maps show that there is a possibility of phase separation between the Mo-rich and W-rich alloys in the presence of Sn. In our Raman spectrum analysis we do not observe the Raman modes corresponding to 2H-SnS_2 single layer at 315 cm^{-1} (A_{1g}) and 205 cm^{-1} (E_g) as they have much lower intensity[27,33] as compared to MoS_2 and WS_2. Hence a direct inference on the Sn concentration in the different regions of the heterostructure is not possible to make from the Raman spectra.

In order to identify the role of Sn in this phase separation, we have studied these samples using STEM. Fig. 3d(i) shows a STEM-HAADF image of the monolayer region in the sample grown with the precursor ratio 1:4:8. The wispy streaks of contrast in the HAADF image come from carbon contamination on the sample, so the image is Fourier-filtered to leave only contributions to the intensity from atoms in the crystal lattice as shown in Fig. 3d(ii).The intensity histogram of the Fourier-filtered image (Fig. 3d(iii)) shows that the region is mostly Mo (large peak at 0.5 relative intensity), but that there are two distinct sub-peaks can be viewed at higher relative intensities of 0.6 and 0.7 (better viewed in the inset) which intuitively correspond to Sn and W. Fig. 3e shows localized regions of the HAADF image and atom-labeled image from Fig. 3d. The difference in intensities between different types of atoms is clearly seen in a line profile across a row which contains each different type of atom. The raw HAADF and the Fourier-filtered image show a distinction between three different classes of atoms. Finally, the thresholds in Fig. 3d(iii) are confirmed through image simulation (Fig. 3f). A continuous lattice of alternating $(Mo/Sn/W)S_2$ is simulated using the same acquisition parameters as used in the microscope. The relative intensities of the

Mo, Sn, and W columns have the same linear progression in intensity as was observed in the histogram in Fig. 3d, which substantiates the atom-labelling performed in Fig. 3d(iv) and demonstrates that the Sn precursor has alloyed into the crystal lattice of the bilayer.

The region shown in Fig. 3d and e are dominated by Mo, however different regions of the same sample, exhibit large compositional differences, and different types of phase segregation in the sample. Fig. 4 contains STEM-HAADF images from two different regions of the sample that demonstrate different growth mechanisms. In Fig. 4a(i), the bilayer is separated into high intensity regions (corresponding to WS_2) and low-intensity regions (corresponding to MoS_2). At the edge of the bilayer, one of the layers has flaked off revealing a monolayer region underneath, revealing that the composition of the bilayer and monolayer regions have the same intensity discrepancies, and not only that are epitaxial to one another. Fig. 4a(ii), on the other hand, shows the same Mo-rich monolayer region from Fig. 3d and 3e, but with an expanded field of view to see the surrounding bilayer regions. The bilayer is observable due to the sharp increase in HAADF intensity (beyond what carbon contamination could account for), as well as the appearance of a distinct Moiré pattern. The Moiré pattern illustrates that here there is no epitaxial relationship between the top and bottom layers here, and that a separate growth mechanism (such as vertical phase segregation) must be responsible for producing the bilayer alloy in this region.

We now put forth the following possible explanation of the observed phase separation and shift towards forming lateral/vertical heterostructures in the presence of Sn. The proposed growth steps and mechanism are shown in supporting information. Without Sn, concentration of nucleation sites on top of the first layer is quite low, resulting in the growth of isolated islands with random orientations whose stoichiometry is not very different from that of the first layer. Due to the high energy of mixing (varying between 0 and 0.72 eV/MX_2 unit, as predicted by our cluster expansion calculations of the $Mo_{1-x}Sn_xS_2$ alloy, Fig. S3) of Sn and MoS_2, addition of Sn yields high concentration of defects in the first layer, which serve as nucleation sites for the second layer. Thus, in the presence of Sn, many secondary islands are more likely to nucleate and grow. As a result, the island boundaries reach each other at much earlier growth stages, when the island size is small. This allows the formation of the experimentally observed monocrystalline second layer through facile re-oriented attachment.[34,35] As the initial concentrations of Sn and Mo precursors are larger, MoS_2 lattice is formed preferentially at first. Subsequently, as the feedstock gas is depleted of Mo and Sn, WS_2 regions form, leading to lateral heterostructures $Mo_{1-x}W_xS_2$ alloys and WS_2. We tested computationally the hypothesis of Sn-substitution defect as a nucleation site for the subsequent growth of the second layer. We prepared a defect with a Sn atom substituting a Mo atom, Sn_{Mo}, using a 15×15 supercell of MoS_2. Due to larger size of Sn atom, Sn substitution creates a strain field of radial compression. The calculated in-plane radial displacement, u_ρ of Mo atoms as a function of the distance ρ from the Sn atom is shown in Fig. 4b. The least square fitting on the log-log plot shown in the inset of Fig. 4b yields the following expression for the radial displacement: $u_\rho = 0.56\rho^{1.4}$. If out of plane motion is allowed, the Sn_{Mo} defect displays out-of-plane buckling of 0.13Å. We next evaluated the effect of Sn_{Mo} on precursor adsorption by comparing adsorption energies using a 8×8 supercell of MoS_2. In our DFT calculations, MoS_2 and WS_2 molecules were considered as typical gas phase precursors. Energies of adsorbed MoS_2 and WS_2 on pristine single-layer 2D MoS_2 and near Sn-substitution defect in 2D MoS_2 were compared. Fig. 4c shows the equilibrium geometry for MoS_2 adsorption on pristine 2D MoS_2. The molecule is positioned directly above the Mo atom and each of the molecule's pair of S atoms is located above the hollow sites of the surface. The calculated adsorption energy of MoS_2 at Sn_{Mo} is 1.0 eV lower than that on the pristine MoS_2 lattice, due to which Sn_{Mo} proves to be an active site for MoS_2 adsorption. The equilibrium geometry is shown in Fig. 4d. The energy difference is significant enough for a large population difference of MoS_2 precursors at pristine and Sn-substituted sites of 2D MoS_2 to exist at the growth temperature of 800^0C. The initial seeding at Sn_{Mo} could further lead to facile nucleation of the second layer. The adsorption of the WS_2 precursor at the pristine 2D MoS_2 and Sn_{Mo} is similar to that of MoS_2 as can be seen from the equilibrium geometries of

WS_2 at these sites shown in Fig. 4e and f respectively. The difference in adsorption energy between the two sites is 1.1 eV. It is larger than that of MoS_2, giving slight preference for the adsorption of WS_2 over MoS_2 at Sn_{Mo}, assuming that chemical potentials of the two precursors are set to give equal populations of MoS_2 and WS_2 on the pristine surface. This difference may serve as an explanation for the vertical phase segregation seen in Fig. 4a(ii). The proposed growth mechanism for the alloys and heterostructures as a function of doping and Sn addition is summarized in the schematic in Fig. 4g.

In conclusion, we have demonstrated that systematic tuning of the initial precursor concentration can engineer the structure which varies from uniform alloy to in-plane heterostructure of the 2D TMDs. By controlling the composition, we can modify the bandgap of the binary alloy TMDs. The experimental and simulation results concludes that the substitution of a non-isomorphous ternary atom in a binary alloy system can result in phase separation to form Mo-rich and W-rich alloy regions and facilitates mutlilayer growth of these alloy heterostructures. This technique of growing alloy heterostructures would be of interest in designing optoelectronic devices with tunable spectral responsivity.

Acknowledgement: This work was supported by the MURI ARO program, grant number W911NF-11-1-0362, by FAME, one of six centers of STARnet, a Semiconductor Research Corporation program sponsored by MARCO and DARPA. This research used resources provided by the Navy DoD Supercomputing Resource Center. This research was partially supported by the Center for Nanophase Materials Sciences (CNMS), which is sponsored at ORNL by the Scientific User Facilities Division, Office of Basic Energy Sciences, U.S. Department of Energy (JAH and JCI).

References

(1) Wang, Q. H.; Kalantar-Zadeh, K.; Kis, A.; Coleman, J. N.; Strano, M. S. *Nat Nano* **2012**, *7*, 699–712.

(2) Mak, K. F.; Shan, J. *Nat Photon* **2016**, *10*, 216–226.

(3) Feng, J.; Qian, X.; Huang, C.-W.; Li, J. *Nat Photon* **2012**, *6*, 866–872.

(4) Hui, Y. Y.; Liu, X.; Jie, W.; Chan, N. Y.; Hao, J.; Hsu, Y.-T.; Li, L.-J.; Guo, W.; Lau, S. P. *ACS Nano* **2013**, *7*, 7126–7131, PMID: 23844893.

(5) He, Y. et al. *Nano Letters* **2016**, *16*, 3314–3320.

(6) Su, S.-H.; Hsu, Y.-T.; Chang, Y.-H.; Chiu, M.-H.; Hsu, C.-L.; Hsu, W.-T.; Chang, W.-H.; He, J.-H.; Li, L.-J. *Small* **2014**, *10*, 2589–2594.

(7) Song, J.-G.; Ryu, G. H.; Lee, S. J.; Sim, S.; Lee, C. W.; Choi, T.; Jung, H.; Kim, Y.; Lee, Z.; Myoung, J.-M.; Dussarrat, C.; Lansalot-Matras, C.; Park, J.; Choi, H.; Kim, H. *Nature Communications* **2015**, *6*, 7817 EP –.

(8) Feng, Q.; Zhu, Y.; Hong, J.; Zhang, M.; Duan, W.; Mao, N.; Wu, J.; Xu, H.; Dong, F.; Lin, F.; Jin, C.; Wang, C.; Zhang, J.; Xie, L. *Advanced Materials* **2014**, *26*, 2648–2653.

(9) Yoshida, S.; Kobayashi, Y.; Sakurada, R.; Mori, S.; Miyata, Y.; Mogi, H.; Koyama, T.; Takeuchi, O.; Shigekawa, H. *Scientific Reports* **2015**, *5*, 14808 EP –.

(10) Kutana, A.; Penev, E. S.; Yakobson, B. I. *Nanoscale* **2014**, *6*, 5820–5825.

(11) Xi, J.; Zhao, T.; Wang, D.; Shuai, Z. *The Journal of Physical Chemistry Letters* **2014**, *5*, 285–291, PMID: 26270701.

(12) Zhang, M.; Wu, J.; Zhu, Y.; Dumcenco, D. O.; Hong, J.; Mao, N.; Deng, S.; Chen, Y.; Yang, Y.; Jin, C.; Chaki, S. H.; Huang, Y.-S.; Zhang, J.; Xie, L. *ACS Nano* **2014**, *8*, 7130–7137, PMID: 24884059.

(13) Chen, Y.; Dumcenco, D. O.; Zhu, Y.; Zhang, X.; Mao, N.; Feng, Q.; Zhang, M.; Zhang, J.; Tan, P.-H.; Huang, Y.-S.; Xie, L. *Nanoscale* **2014**, *6*, 2833–2839.

(14) Chen, Y.; Xi, J.; Dumcenco, D. O.; Liu, Z.; Suenaga, K.; Wang, D.; Shuai, Z.; Huang, Y.-S.; Xie, L. *ACS Nano* **2013**, *7*, 4610–4616, PMID: 23600688.

(15) Geim, A. K.; Grigorieva, I. V. *Nature* **2013**, *499*, 419–425.

(16) Gong, Y. et al. *Nat Mater* **2014**, *13*, 1135–1142.

(17) Gong, Y.; Lei, S.; Ye, G.; Li, B.; He, Y.; Keyshar, K.; Zhang, X.; Wang, Q.; Lou, J.; Liu, Z.; Vajtai, R.; Zhou, W.; Ajayan, P. M. *Nano Letters* **2015**, *15*, 6135–6141, PMID: 26237631.

(18) Rivera, P.; Schaibley, J. R.; Jones, A. M.; Ross, J. S.; Wu, S.; Aivazian, G.; Klement, P.; Seyler, K.; Clark, G.; Ghimire, N. J.; Yan, J.; Mandrus, D. G.; Yao, W.; Xu, X. *Nature Communications* **2015**, *6*, 6242 EP –.

(19) Lee, C.-H.; Lee, G.-H.; van der Zande, A. M.; Chen, W.; Li, Y.; Han, M.; Cui, X.; Arefe, G.; Nuckolls, C.; Heinz, T. F.; Guo, J.; Hone, J.; Kim, P. *Nat Nano* **2014**, *9*, 676–681.

(20) Wang, G.; Robert, C.; Suslu, A.; Chen, B.; Yang, S.; Alamdari, S.; Gerber, I. C.; Amand, T.; Marie, X.; Tongay, S.; Urbaszek, B. *Nature Communications* **2015**, *6*, 10110 EP –.

(21) Tongay, S.; Narang, D. S.; Kang, J.; Fan, W.; Ko, C.; Luce, A. V.; Wang, K. X.; Suh, J.; Patel, K. D.; Pathak, V. M.; Li, J.; Wu, J. *Applied Physics Letters* **2014**, *104*, 012101.

(22) Lee, Y.-H.; Zhang, X.-Q.; Zhang, W.; Chang, M.-T.; Lin, C.-T.; Chang, K.-D.; Yu, Y.-C.; Wang, J. T.-W.; Chang, C.-S.; Li, L.-J.; Lin, T.-W. *Advanced Materials* **2012**, *24*, 2320–2325.

(23) Zhan, Y.; Liu, Z.; Najmaei, S.; Ajayan, P. M.; Lou, J. *Small* **2012**, *8*, 966–971.

(24) Liu, K.-K.; Zhang, W.; Lee, Y.-H.; Lin, Y.-C.; Chang, M.-T.; Su, C.-Y.; Chang, C.-S.; Li, H.; Shi, Y.; Zhang, H.; Lai, C.-S.; Li, L.-J. *Nano Letters* **2012**, *12*, 1538–1544, PMID: 22369470.

(25) Kobayashi, Y.; Mori, S.; Maniwa, Y.; Miyata, Y. *Nano Research* **2015**, *8*, 3261–3271.

(26) Zheng, S.; Sun, L.; Yin, T.; Dubrovkin, A. M.; Liu, F.; Liu, Z.; Shen, Z. X.; Fan, H. J. *Applied Physics Letters* **2015**, *106*, 063113.

(27) Huang, Y.; Sutter, E.; Sadowski, J. T.; Cotlet, M.; Monti, O. L.; Racke, D. A.; Neupane, M. R.; Wickramaratne, D.; Lake, R. K.; Parkinson, B. A.; Sutter, P. *ACS Nano* **2014**, *8*, 10743–10755, PMID: 25247490.

(28) Lee, C.; Yan, H.; Brus, L. E.; Heinz, T. F.; Hone, J.; Ryu, S. *ACS Nano* **2010**, *4*, 2695–2700, PMID: 20392077.

(29) Berkdemir, A.; Gutiérrez, H. R.; Botello-Méndez, A. R.; Perea-López, N.; Elías, A. L.; Chia, C.-I.; Wang, B.; Crespi, V. H.; López-Urías, F.; Charlier, J.-C.; Terrones, H.; Terrones, M. *Scientific Reports* **2013**, *3*, 1755 EP –.

(30) Peimyoo, N.; Shang, J.; Cong, C.; Shen, X.; Wu, X.; Yeow, E. K. L.; Yu, T. *ACS Nano* **2013**, *7*, 10985–10994.

(31) Sun, Q. C.; Yadgarov, L.; Rosentsveig, R.; Seifert, G.; Tenne, R.; Musfeldt, J. L. *ACS Nano* **2013**, *7*, 3506–3511.

(32) Krivanek, O.; Corbin, G.; Dellby, N.; Elston, B.; Keyse, R.; Murfitt, M.; Own, C.; Szilagyi, Z.; Woodruff, J. *Ultramicroscopy* **2008**, *108*, 179 – 195, Proceedings of the Sixteenth International Microscopy Congress.

(33) Su, G.; Hadjiev, V. G.; Loya, P. E.; Zhang, J.; Lei, S.; Maharjan, S.; Dong, P.; M. Ajayan, P.; Lou, J.; Peng, H. *Nano Letters* **2015**, *15*, 506–513, PMID: 25494406.

(34) Penn, R. L.; Banfield, J. F. *Science* **1998**, *281*, 969–971.

(35) Artyukhov, V. I.; Hu, Z.; Zhang, Z.; Yakobson, B. I. *Nano Letters* **2016**, *16*, 3696–3702, PMID: 27187078.

Figure caption

Fig 1: (a) Schematic of growth of TMDC alloys and heterostructures. Optical micrographs of samples grown from binary metal precursors, MoO_3 and WO_3 in the ratio 1:2, 1:4 and 1:6 (b) and from ternary metal precursors, MoO_3, WO_3 and SnO_2 in the ratio 1:2:8, 1:4:8 and 1:6:8 (c). Scale bar = 10μm. AFM images and step height analysis for samples grown from binary (d) and ternary (d) metal precursors.

Fig 2: (a) (i) Optical (ii) Raman and (iii) PL characterization of the sample grown from binary precursor mixture in the ratio 1:2. Scale bar = 5μm. Raman spectra at the points marked in red and black in (i) is shown along with maps obtained at 350 cm^{-1} (green) and 405 cm^{-1} (red). The combined PL map at 1.82 and 1.9eV is plotted. (b) Raman spectra (i), Raman maps at 350 cm^{-1} (green) and 405 cm^{-1} (red) (ii) and PL map at 1.85 eV (iii) of the sample grown from binary precursor mixture in the ratio 1:4 whose optical micrograph is shown in the inset (i). Scale bar = 5μm. (c) (i) Raman spectra obtained for the sample grown from precursor ratio 1:6 is shown at the two regions marked in red (center) and black (edge) in the optical micrograph in inset is shown. Scale bar = 10μm. (ii) Raman map overlay and (iii) PL maps at 1.82 (red) and 1.9 (green) eV is shown. (d) (i) HAADF-STEM image of large region of bilayer $Mo_{1-x}W_xS_2$ binary alloy. The image on the lower right shows a higher magnification image where the difference in intensity between the Mo and W atoms can be clearly seen from the line profile across a row of atoms. (ii) In order to attempt to quantify the relative concentrations of Mo and W, a threshold in HAADF intensity is set at the ad hoc relative intensity value of 0.36. The resulting concentration is W-985 atoms (17.2%) and Mo-4736 (82.8%). (iii) From the 0.36 threshold the HAADF image is most faithfully recreated and the atom positions are plotted by type - Mo (blue) and W (yellow).

Fig 3: (a) The PL (i) and Raman (ii) spectra for the ternary sample grown from precursor ratio 1:2:8 is shown at the two regions marked in red and black in the optical micrograph in inset. Scale bar = 10μm. The Raman maps obtained at 350 cm^{-1} (green) and 405 cm^{-1} (red) shown in the inset reveals WS_2 segregation at the edges. (b) The optical (i), Raman (ii) and PL (iii) characterization of the sample grown from ternary precursor mixture in the ratio 1:4:8. Scale bar = 20μm. Raman maps obtained at 350 cm^{-1} (green) and 405 cm^{-1} (red) and their combination map is shown in the top panel while the bottom panel shows the Raman spectra and (iii) shows the PL spectra acquired at the three points shown in (i) indicated by blue, red and black dots. (c) Optical micrograph (i), PL map at 1.94 eV and Raman spectra (iii) of the sample grown from ternary precursor mixture in the ratio 1:6:8. Scale bar = 5μm. The Raman map at 350 cm^{-1} and spectra acquired at the two points indicated in (i) shows bilayer W-dominated alloy at the center. (d) (i) High resolution STEM-HAADF image of the monolayer region obtained from samples grown from 1:4:8 precursor ratio. (ii) Fourier filtered HAADF image showing contributions to the intensity from atoms in the crystal lattice alone. (iii) From the Fourier-filtered image the locations and intensities of all the atoms are found, and a histogram of the different Z-contrasts is plotted showing three distinct peaks at relative intensity values of 0.5, 0.6 and 0.7 (seen more clearly in the inset), which seem to correspond to Mo, Sn, and W atoms. Gaussian fit to these peaks is shown from which thresholds are set at the crossover point of the fitted peaks. (iv) Map obtained from the threshold showing the type of atom at each site is shown over the top of the Fourier-filtered image with Mo in blue, Sn in red and W in yellow. (e) Localized regions of HAADF image (i) along with atom-labelled image from Fig. 3d(ii). The line profile across a row of atoms shows the differences in intensity between Mo, Sn and W atoms as shown in raw and Fourier-filtered image. (f) The threshold chosen to distinguish between atoms is validated through HAADF image simulation of a continuous lattice of alternating $(Mo/Sn/W)S_2$ using same experimental acquisition parameters.

Fig 4: (a) (i) Example of lateral phase segregation. In this region, the bilayer is shown to split into high-contrast regions (WS_2) and low-contrast regions (MoS_2) that are epitaxial at both the monolayer and bilayer levels. (ii) Example of vertical phase segregation showing MoS_2-rich monolayer region and a rotated bilayer region of MoS_2/WS_2 heterostructure. (b) Calculated in-plane radial displacement u_ρ of Mo atoms as a function of the distance ρ from the Sn in Sn-substitution defect Sn_{Mo} in 2D MoS_2. The inset shows the log-log plot with least square fit giving the dependence $u_\rho = 0.56\rho^{1.4}$. Equilibrium geometries of (c) MoS_2 molecule on pristine single layer 2D MoS_2, (d) MoS_2 molecule near Sn-substitution defect Sn_{Mo} in 2D MoS_2, (e) WS_2 on pristine single layer 2D MoS_2, (f) WS_2 molecule near Sn-substitution defect Sn_{Mo} in 2D MoS_2. Blue, yellow, red, and grey spheres designate Mo, W, Sn, and S atoms, respectively. (g) Proposed growth mechanism for the alloys and heterostructures.

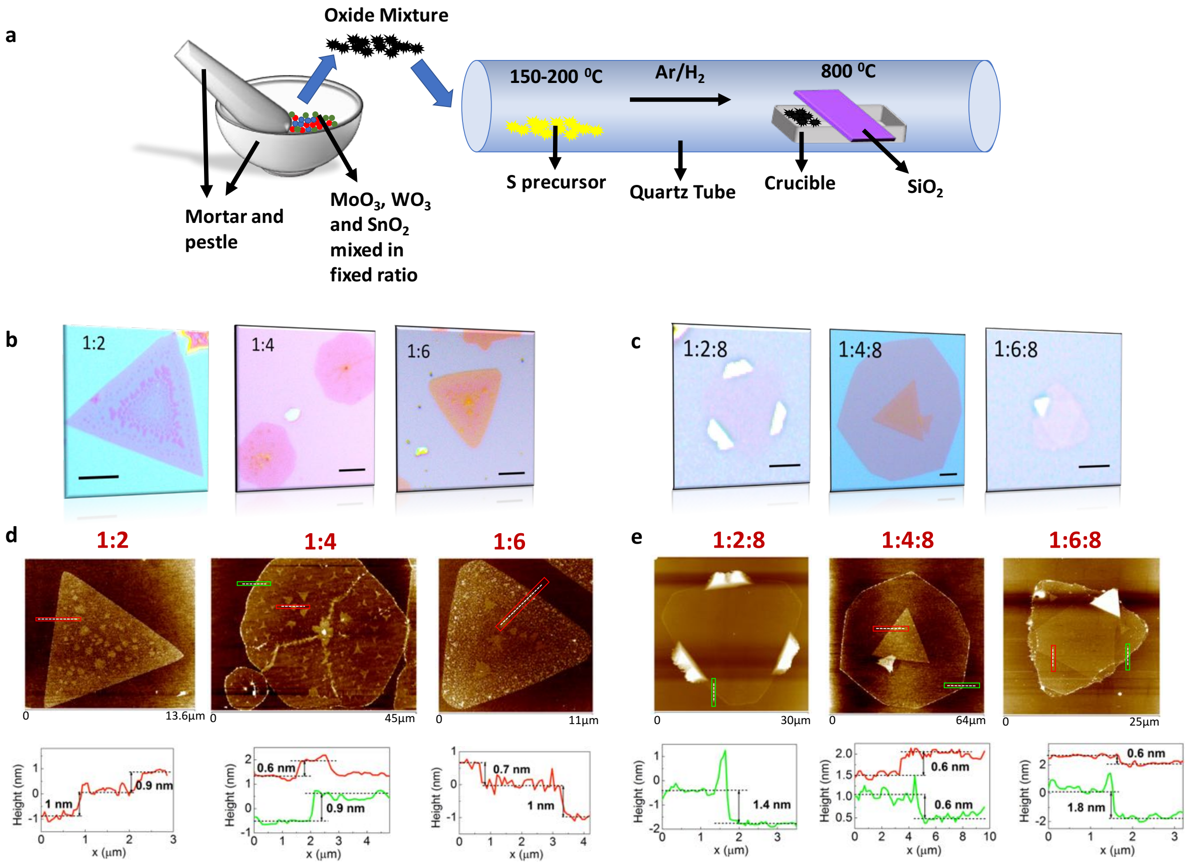
a
Oxide Mixture
150-200 ⁰C
Ar/H₂
800 ⁰C
Mortar and pestle
MoO₃, WO₃ and SnO₂ mixed in fixed ratio
S precursor
Quartz Tube
Crucible
SiO₂
b
1:2
1:4
1:6
c
1:2:8
1:4:8
1:6:8
d
1:2
1:4
1:6
0
13.6µm
45µm
11µm
e
1:2:8
1:4:8
1:6:8
30µm
64µm
25µm
Height (nm)
x (µm)
1 nm
0.9 nm
0.6 nm
0.9 nm
0.7 nm
1 nm
1.4 nm
0.6 nm
0.6 nm
0.6 nm
1.8 nm

Figure 1

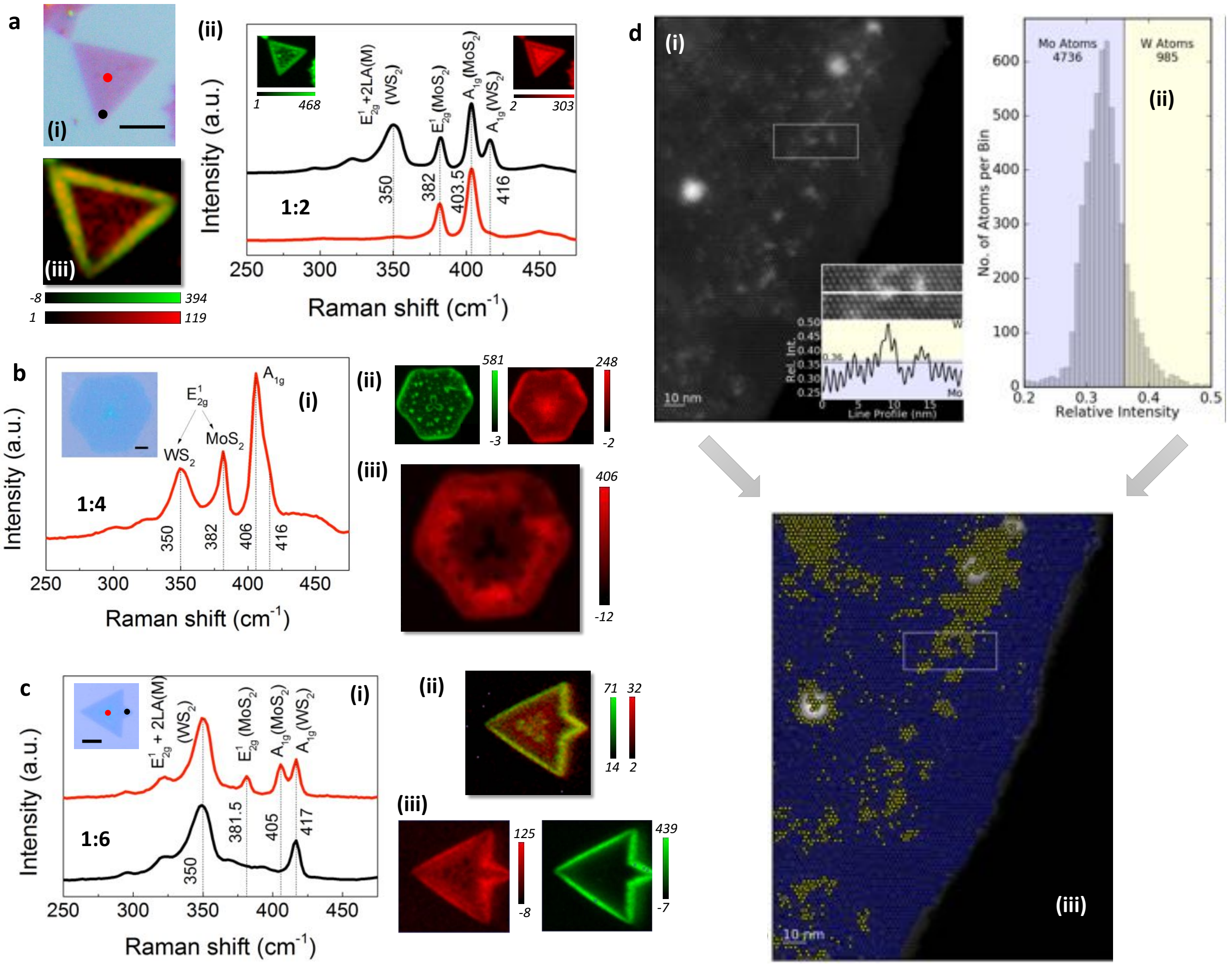
a
(i)
(ii)
(iii)
-8
394
1
119
1
468
2
303
E^1_{2g} +2LA(M) (WS_2)
E^1_{2g} (MoS_2)
A_{1g} (MoS_2)
A_{1g} (WS_2)
350
382
403.5
416
1:2
Intensity (a.u.)
Raman shift (cm^{-1})
250
300
350
400
450
b
E^1_{2g}
WS_2
MoS_2
A_{1g}
1:4
406
581
-3
248
-2
-12
c
E^1_{2g} + 2LA(M) (WS_2)
381.5
405
417
1:6
71
14
32
2
125
-8
439
-7
d
10 nm
Rel. Int.
Line Profile (nm)
W
Mo
0.36
Mo Atoms 4736
W Atoms 985
No. of Atoms per Bin
Relative Intensity
0.2
0.3
0.4
0.5

Figure 2

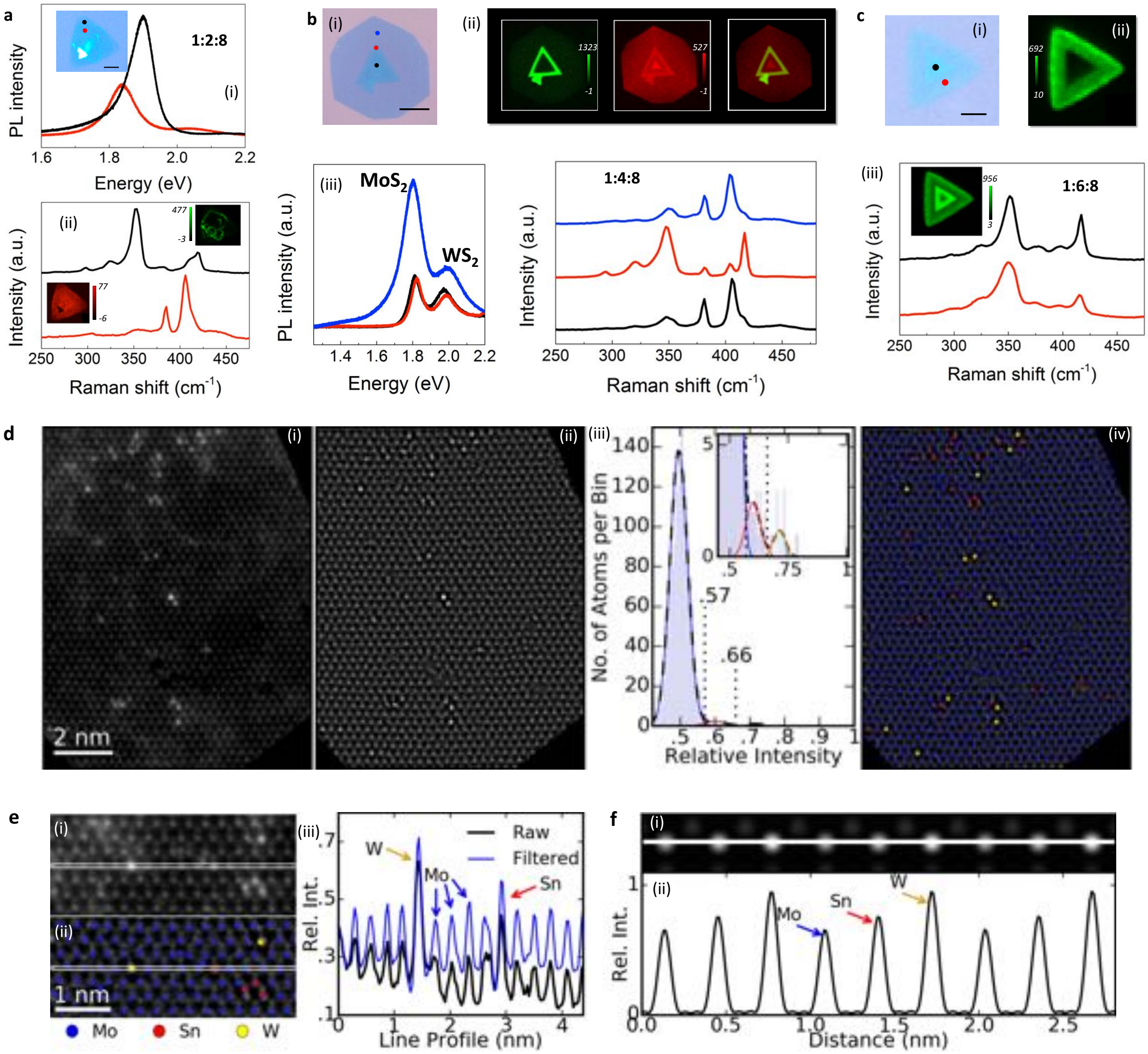
a
1:2:8
(i)
PL intensity
1.6
1.8
2.0
2.2
Energy (eV)
(ii)
477
-3
77
-6
Intensity (a.u.)
250
300
350
400
450
Raman shift (cm^{-1})
b
(i)
(ii)
1323
-1
527
-1
(iii)
MoS_2
WS_2
PL intensity (a.u.)
1.4
1.6
1.8
2.0
2.2
Energy (eV)
1:4:8
Intensity (a.u.)
250
300
350
400
450
Raman shift (cm^{-1})
c
(i)
(ii)
692
10
(iii)
956
3
1:6:8
Intensity (a.u.)
250
300
350
400
450
Raman shift (cm^{-1})
d
(i)
2 nm
(ii)
(iii)
No. of Atoms per Bin
140
120
100
80
60
40
20
0
.57
.66
.5
.6
.7
.8
.9
1
Relative Intensity
5
0
.5
.75
1
(iv)
e
(i)
(ii)
1 nm
Mo
Sn
W
(iii)
Raw
Filtered
W
Mo
Sn
Rel. Int.
.7
.5
.3
.1
0
1
2
3
4
Line Profile (nm)
f
(i)
(ii)
1
Mo
Sn
W
Rel. Int.
0
0.0
0.5
1.0
1.5
2.0
2.5
Distance (nm)

Figure 3

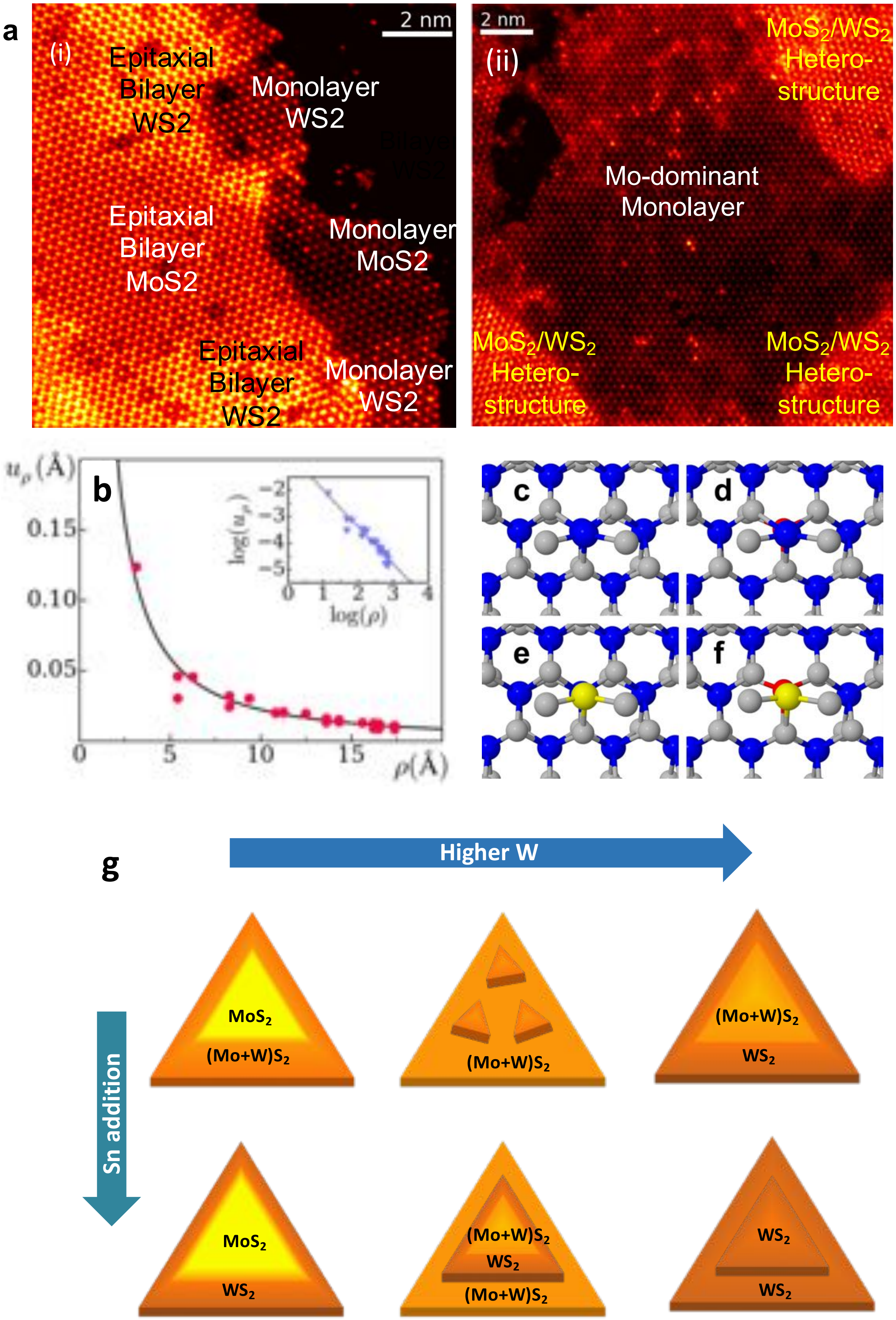
a
(i)
2 nm
Epitaxial Bilayer WS2
Monolayer WS2
Bilayer WS2
Epitaxial Bilayer MoS2
Monolayer MoS2
Epitaxial Bilayer WS2
Monolayer WS2
(ii)
2 nm
MoS_2/WS_2 Hetero-structure
Mo-dominant Monolayer
MoS_2/WS_2 Hetero-structure
MoS_2/WS_2 Hetero-structure
b
u_ρ (Å)
0.15
0.10
0.05
0
5
10
15
ρ(Å)
$\log(u_\rho)$
-2
-3
-4
-5
0
1
2
3
4
$\log(\rho)$
c
d
e
f
g
Higher W
Sn addition
MoS_2
$(Mo+W)S_2$
$(Mo+W)S_2$
$(Mo+W)S_2$
WS_2
MoS_2
WS_2
$(Mo+W)S_2$
WS_2
$(Mo+W)S_2$
WS_2
WS_2

Figure 4